Numerical Investigation of Parietal Pressure Distribution on NACA-0012 Wing Controlled by Micro-cylindrical Rod Arranged in Tandem

Abderrahim Larabi, Michael Pereira, Florent Ravelet, T. Azzam, Hamid Oualli, Mahmoud Mekadem, L. Menfoukh, F. Bakir

Noname manuscript No.
(will be inserted by the editor)

Numerical Investigation of Parietal Pressure Distribution on NACA-0012 Wing Controlled by Micro-cylindrical Rod Arranged in Tandem

Abderrahim LARABI · Michael PEREIRA · Florent RAVELET · Tarik AZZAM · Hamid OUALLI · Mahmoud MEKADEM · Laiche MENFOUKH · Farid BAKIR

Received: date / Accepted: date

Abstract The primary aim of this study is to investigate the influence of an upstream cylindrical rod on the laminar separated boundary layer that develops on a symmetrical profile wing operating at a Reynolds number of $Re_c = 4.45 \times 10^5$. To get further insight onto the aerodynamic performances of this wing at low Reynolds number, numerical simulations with a transitional turbulence model are performed with the ANSYS-Fluent software. The passive flow control technique is applied by setting up a cylindrical rod of diameter d upstream of a NACA-0012 airfoil of chord lenght c. The dimensionless rod diameter with respect to the chord length is $d/c = 2/150$. Simulations are carried out over a wide range of angles of attack for both the baseline case and the controlled case by the passive proposed technique. The effects of the wing incidence on the parietal pressure distributions on the suction surface of the wing are examined. The results show that the Laminar Separation Bubble that is formed on the upper surface is moving upstream toward the leading edge as the incidence is increased. Moreover, qualitative analysis of the transition zone revealed that presence of the wing in the rod wake exerted considerable effect on the pressure coefficient. Particularly, this passive turbulence generator contributes to eliminate the boundary layer separation by forcing the shear layer to stick to the wing surface over a significant extent, resulting in a mean drag dropping of 73% at 12° incidence, and a lift enhancement of about 23% at an angle of attack of 15°.

Keywords Laminar separated flow · Passive control · Bodies wake interaction · NACA0012 airfoil · Drag reduction · Lift enhancement.

A. LARABI · T. AZZAM · H. OUALLI · M. MEKADEM · L. MENFOUKH
Fluid Mechanics Laboratory, EMP, BP 17 Bordj El Bahri, Algiers, 16111, Algeria

M. PEREIRA · F. RAVELET · F. BAKIR
Arts et Metiers Institute of Technology, CNAM, LIFSE, HESAM University, F-75013 Paris, France
Tel.: (+33)-144246396
E-mail: farid.bakir@ensam.eu

1 Introduction

The laminar separation bubble is one of the major issues met in several industrial applications, in particular those operating at low Reynolds numbers such as UAV (Unmanned Air Vehicle), Micro Air Vehicle, Race Cars and even Wind Turbines. The boundary layer transition mechanism from laminar to turbulent state of such winged devices is deeply influenced by the aerodynamic characteristics of the wing in terms of boundary layer thickness, transition and separation locations, and wake thickness. In particular, the dynamic behavior underlying behind these low Reynolds flows showed occurrence of slowly recirculating fluid characterized by a stationary rotating swirl known as a Laminar Separation Bubble (LSB) identified to be responsible for several negative effects on the overall aerodynamics performances, such as lift decreasing, drag increasing, aircraft stability reducing, vibration, and even disturbing noise. This separation bubble is basically developed when the laminar boundary layer cannot overcome the local flow deceleration just coming after its acceleration. Hence, when it bypasses the leading edge of the wing the boundary layer peels off from the wall surface under the influence of an adverse pressure gradient. However, at higher Reynolds numbers this laminar boundary layer grows drastically to a turbulent state

due to the presence of large inertial forces, and is therefore better able to overcome this adverse pressure gradient. After that, the development of Kelvin-Helmholtz instabilities in this separated shear layer initiates turbulence which yields three-dimensional flow motions. This turbulent mixing is a complex process resulting in the separated streamline reattachement, through interactions between turbulent motions and the wing that incites the reattachment of the separated shear layer to the airfoil surface, leaving an enclosed region of dead recirculating air. Therefore, understanding the physics involved in this phenomenon and the possibility to control the resulting bubble are determinant for efficient engineering design.

Yang *et al.* [1] used numerical simulations based on RANS-LES turbulence model to compare the time-averaged and instantaneous flow-field near the airfoil surface close to the separation region. Their main results show that typical Kelvin-Helmholtz instabilities in the shear layer are twisting into vortices that force the separated flow to stick towards the wall surface leading to a bubble shape in the time averaged outcome. Moreover, the experimental results presented by Hain *et al.* [2] with PIV measurements at a low Reynolds number flow around a SD7003 airfoil point out the existence of a shear layer rolling up into a vortex sheet in the separated boundary layer originating from the presence of Kelvin-Helmholtz instabilities just after triggering of the boundary layer transition. Zhang *et al.* [3] conducted a hot wire investigation on the suction side of a wing at low Reynolds number which showed that a transient boundary layer can reattach to form a bubble and then evolves into fully turbulent state. A review on laminar separation bubbles is presented by Tani [4] where the effects of the Reynolds number on the laminar separation bubble occurrence are discussed. The bubble is observed to appear for a Reynolds number ranging in between $[6 \times 10^4 - 6 \times 10^6]$. Russell [5] introduced a theoretical model characterizing the laminar separation bubble in which he advocated a way of depicting the different critical points describing the LSB throughout the on-surface pressure measurements. The analysis clearly shows that pressure distribution on the suction side remains fairly constant when the laminar boundary layer separates, after that the boundary layer reattaches to the surface when shear layer transition is triggered as revealed by drastically pressure increase. Hu *et al.* [6] conducted time averaged and instantaneous PIV experiments to provide information about the transient behavior of the laminar separated flow on low speed NASA GA (W-1) airfoil at a Reynolds number of 7×10^4. It is found that the bubble appears only when the incidence is in the range $[8^\circ - 11.8^\circ]$. Above this range at around 12° the pressure gradient becomes so significant that it induces sudden bubble brust, causing the complete stalling of the airfoil. The authors reported also that LSB moves upstream towards the leading edge as the incidence increases in such a way its overall length remains unchanged. The laminar portion of this bubble, however, slightly extends in size, and the turbulent portion shrinks with the increasing angle of attack.

A literature review on flow control shows the existence of several techniques to manoeuvre a boundary layer, either in purpose of flow separation postponement so that the flow remains attached to the airfoil surface, or to achieve lift enhancement, drag decreasing and noise damping. The flow control techniques are categorized into two major classes: active and passive techniques. Gad el Hak [7] added a reactive class to the above and showed up more specific ways of control depending upon the sought main goal. A good flow control technique with such a control device needs to be simple to implement, cheap and keeping the overall geometry unchanged. For these reasons, the so-called passive control techniques are the most widely used for simplicity, affordness and do not require any external energy supplying.

Several numerical and experimental studies on passive control of laminar separated flows have been carried out around different airfoils. Zhang *et al.* [8] experimentally investigated aerodynamic performances of a cylinder placed downstream a NACA-4412 airfoil at low Reynolds numbers ranging between $[1.47 \times 10^4 - 1.4 \times 10^5]$. They pointed out an abrupt decrease in both lift and drag forces as the side distance is increased. Zhou *et al.* [9] examined numerically the wake body interaction between a cylinder placed in the near wake of NACA-4412 airfoil for a Reynolds number of 200 based on the cylindrical body diameter. The main outcomes indicate a significant impact on the aerodynamic loadings, vortex patterns and shedding frequencies acting on the cylinder with an upstream streamlined body. An exhaustive review on the effects of wakes interaction and shedding frequencies between the added bluff body and the cambered airfoil arranged in tandem was given by Bajalan *et al.* [10]. The findings highlighted the global physical involved phenomena when the airfoil wake interact with the cylinder body. This mutual interference led to a significant change in Strouhal number values of both obstacles and the vortex patterns depending upon the spacing between them. Shan *et al.* [11] focused their numerical investigation on both passive and active vortex generators used to control the flow separation over NACA-0012 airfoil at 6° incidence angle. The results showed a reduction of the separation zone over a sig-

nificant extent up to 80% when the passive vortex generator is added. On the other hand, the active vortex generator made the separation zone almost to vanish in the time averaged flow results. However, this control technique did not impart drag reduction neither lift enhancement. Igarashi *et al.* [12,13,14] suggested a control method of the separated shear layer from bluff bodies by placing a cylindrical rod in tandem arrangement in the upstream crossflow. The idea consisted in forcing the free shear layer to reattach on the body surface. This technique was applied to a cylinder, flat plate, square prism, diamond arranged square prism in order to investigate the flow response to this control method. The outcome recorded a pressure drag reduction of 63%, 30%, 75% and 34% respectively to each bluff body compared to the baseline bodies. Hafien *et al.* [15] carried out numerical simulations to consider the effect of self adapting flexible flaps on flow separation over NACA-0012 airfoil at moderate Reynolds number. The results showed a large modification of flow structure when elastic flap deforms under fluid- structure interaction forcing the wake to reduce in size and to lower intensity for shedding vortices. This resulted in a maximum lift enhancement of 69.49% for variable length flaps. Fan *et al.* [16] investigate by LES the effect of turbulence generated by a rod of 10 mm in diameter in front of a wavy leading edge wing on its broadband noise for Reynolds number of 3.97×10^5. Results showed the fluctuations of lift and drag coefficients are damped out by 65.4% and 71.4% respectively causing a substantial reduction in the mean noise of 9.5 dB. Supreeth et al. [17] highlighted the effectiveness of vortex generators in the shape of tubercles on the overall wing performances of a S823 airfoil. They postulated the main part of tubercles in smoothening and mitigating the stall effects to higher incidences which widen the scope of engineering operations for this modified wing. Moreover, the technique offered an additional increase of 19.38% in the overall aerodynamic efficiency. Sefiddashti *et al.* [18] conducted experimental investigation to assess the aerodynamic performances of Riso airfoil based wing controlled by a micro-riblets placed on its suction surface at wide range of angles of attack. They showed a significant drag reduction of 29.7% and 54% for Reynolds numbers of 2.02×10^5 and 1.4×10^5 respectively, which occurred at 7° incidence. Durhasan [19] studied experimentally the laminar separation bubble flow mechanism at pres-stall regime for SD7062 airfoil controlled by small rod of different diameters at Reynolds number of 3×10^4 placed on the suction side at various chordwise locations. The PIV results revealed significant reduction in the size of LSB for proper rod diameter and location, along with decrease in height of the boundary layer by 22% which is coherent with the correlated reduction of 34% in the eddies' turbulent energy in the flow.

Overall, the major part of the numerical studies are carried out only with fully turbulent classical RANS models (Spallart-Almaras, $k-\epsilon$ and $k-\omega$ SST). The primary purpose of this study is to allow further insights into the fundamental knowledge behind the laminar separated boundary layer on a symmetrical airfoil at low Reynolds number using a transition sensitive RANS turbulence model known as Transition SST ($\gamma - \tilde{Re}_{\theta,t}$). In addition, a cylindrical rod is set upstream of the NACA0012 airfoil to control the separated flow around it. It is aimed to assess the feasibility of such a passive control technique and establish the optimum size and location of the rod to enhance aerodynamic performances of the considered wing.

2 Numerical Method

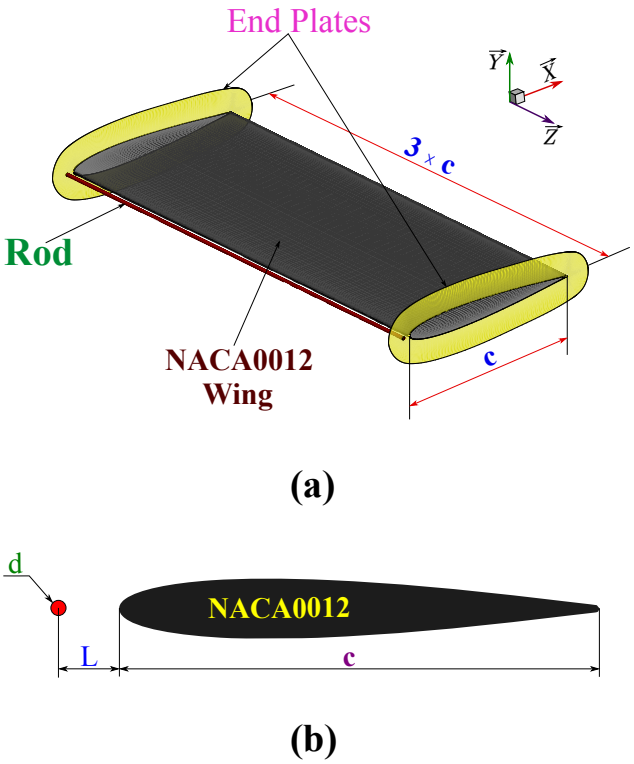

Fig. 1 Schematic of the NACA-0012 wing of chord length c controlled by a micro-cylinder of diameter d placed at a distance L upstream of the leading edge

2.1 Geometry

The profile which is studied and the geometrical arrangment of the passive control are sketched in Fig. 1. Preliminary experiments have been performed in a wind tunnel. The exeprimental profile consists of a symmetric NACA-0012 profile with a chord length $c = 150$ mm and a span equals to $3 \times c = 450$ mm. It has two lateral endplates. The cylinder of circular cross-section with diameter $d = 2$ mm is placed $L = 3 \times d = 6$ mm upstream of the leading edge of the profile. This distance has been chosen for the following reason:

Under the flow conditions of the study, *i.e.* with a freestream velocity of 43.3 m.s^{-1}, the Reynolds number based on the micro-cylinder diameter is $Re_d = 5931$. According to Norberg [20], the formation length of the Von-Karman vortex street behind this tiny cylinder at this Reynolds number is roughly equals to $2 \times d$. The purpose behind setting the distance L at three times the rod diameter is thus to be as close as possible to the vortex formation length.

2.2 Computational Domain

The three-dimensional computational domain used to carry out this numerical study is illustrated in Fig.2. The coordinate system origin is placed at the leading edge of the wing. The overall domain dimensions are $42 \times c$ in lenght, $24 \times c$ m in height and $3 \times c$ in width. The inlet boundary condition of the main domain is $12 \times c$ upstream of the airfoil. The domain extension has been chosen in order to maintain a low blockage level and to ensure as little influence of all the domain boundaries as possible; a sensitivity test has been performed to optimize calculations in terms of time, memory and cost. The final domain gives a discrepancy of less than 1% in terms of aerodynamic force with respect to the experiment.

2.3 Mesh Generation

The adopted grid topology for the considered computational domain is generated using ANSYS-Meshing commercial software as illustrated in Fig.2.In order to construct a high-quality structured mesh, the domain is divided into several blocks allowing finer mesh in regions of susceptible eddies formation and coarse grid in far field regions. This strategy is performed using interface boundary conditions between different blocks. Furthermore, to reduce the overall skewness and to ensure better cells orthogonality for the near wall grid elements as density is increased for the following mesh dependence analysis, an O-grid type topology is adopted and centerd around both the wing and the cylindrical rod. This approach gives a smooth mesh transition in the leeward zone of the rod to the leading edge of the wing and allows a high resolution of the boundary layer while keeping relatively a low cell counts compared to C-grid type topology used in former similar studies which showed a reduction of about 50% in mesh size. The structured quadrilateral elements are chosen for the whole computational domain since they provide a high flexibility to control the cell counts with low memory consumption, accurate flow resolution and good flow alignment with respect to the mesh cells thus the overall rate of solution convergence is increased. Refined quadrilateral meshes are applied to critical flow zones where most important phenomena affecting the flow structure around the wing are recorded. These zones are mainly the leeward side of the rod where the vortex shedding interacts with the leading edge of the wing ensuring thus minimization of the numerical viscosity effect responsible of artificial dissipation of the shedded vortices. In addition, a particular attention is paid to the mesh refinement at the airfoil suction side to capture accurately flow features (Laminar Separation Bubble) involved in vicinity of the wing airfoil including leading and trailing edges. In order to assess the significant impact of grid density on accuracy and convergence rate of the numerical solution, three different grid sizes are investigated for the mesh dependency analysis (Tab. 1). The coarse grid (MESH-1) contains 200 points on the suction side of the airfoil, the fine mesh (MESH-2) with 450 grid points and the refined grid (MESH-3) has 640 points. It is noticed throughout sensitivity assessment for lift coefficient force that a deviation of about 4.59% is recorded for the coarse (MESH-1) and fine (MESH-2) meshes. While for the refined mesh (MESH-3), this difference in c_L drops to reach a value of roughly 0.56%. As a result, MESH-2 is retained and found to be suited to achieve accurately enough results for this numerical investigation. Another important grid independence was found to be in the exposure of turbulence models to y^+ values. Values of y^+ less than unity found to be necessary in order to capture transitional features of the flow on the suction side of the airfoil by accurately modelling the boundary layer. A target value of 0.7 based on the freestream inlet velocity is applied to the entire wing surface and the cylindrical rod during pre-processing simulation case. After that, y+ distribution along the extrados and intrados of the airfoil and around the cylinder circumference is checked in post-processing phase for all simulations and showed to be less than unity. A total of 15 inflation layers were chosen with a stretching ratio of 18% at the wall surface

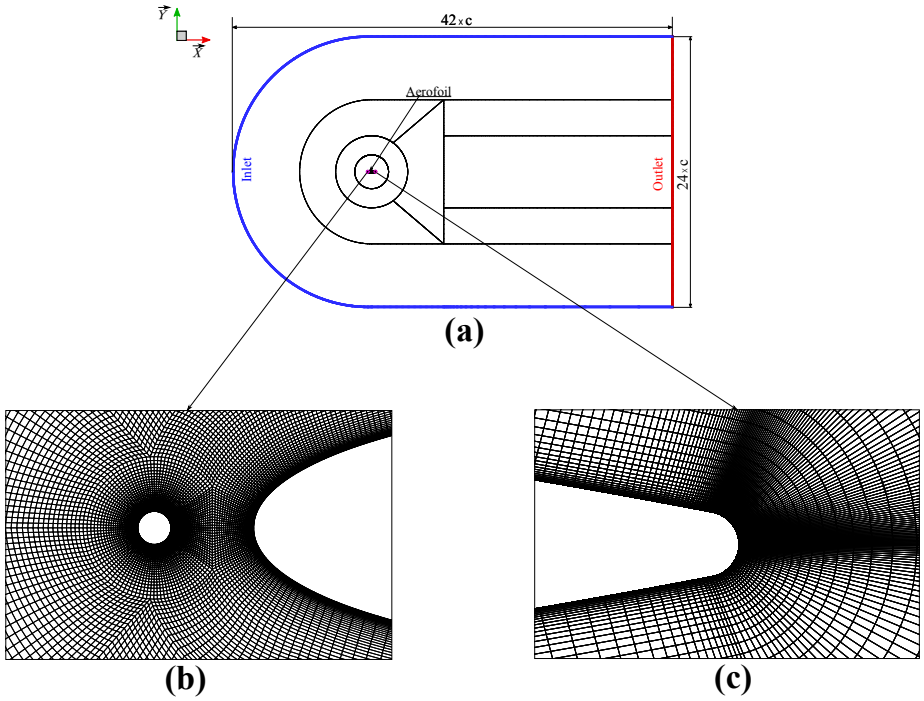

Fig. 2 (a) Schematic of adopted mesh topology for the domain(b) Structured mesh around the rod close to the airfoil, (c) Structured mesh close to the trailing edge of the airfoil.

Table 1 Grid independence analysis

Mesh	Nodes on Aerofoil	c_L at 10°	Error (%) with previous mesh
MESH-1	200	0.8636	-
MESH-2	450	0.9035	4.59
MESH-3	640	0.9086	0.56

giving a prism layer thickness large enough to fit development of the boundary layer along with the separation bubble that may occur. As a result of this parametric strategy, a reasonable quality and sufficiently fine structured mesh is with solution-mesh independency condition satisfied.

2.4 Turbulence Model

The conventional turbulence models available for RANS formulation such as the one equation Spalart-Allmaras model and ther two equations $k-\epsilon$ and $k-\omega$ models, do not include laminar effects especially for low Reynolds number flows. Even though, DNS and LES methods solve turbulence with sufficient precision so that laminar and transition effects can be predicted, grid density and time resolution requirements are prohibitive and probably inappropriate to be used for industrial design purposes. This led to an attempt to include laminar transitional effects using damping functions in near wall regions to gain relatively good prediction of transition by diffusing freestream turbulence into the boundary layer. In addition, this strategy offers a good balance between grid density requirement and flow complexity. This model known as Transition Shear Stress Transport ($\gamma - \tilde{Re}_{\theta,t}$) for Low Reynolds number approach introduces a so-called viscosity limiter that reduces prediction of the wall shear stress thus it is more likely to get separation over smooth surface and results will give better agreement with experiments of separated flows. Several RANS turbulence models are used to investigate laminar separated flows at low Reynolds numbers. It is noticed that Transition SST model provided good prediction of pre and post stall behavior for aerodynamic loads and is in good agreement with correlating comparative wind tunnel experiments. Furthermore, this latter model proved its reliability in capturing flow interaction features between bodies and its high revelation of parietal pressure oscillations. According to what has been discussed so far, it seems that Transition SST turbulence model is capable of capturing accurately laminar separation with transition of the boundary layer on wings operating at low Reynolds flow regime, allowing to solve details inside the boundary layer when blending effectively between the standard $k-\omega$ in near wall regions and $k-\epsilon$ model in the far field. Hence, Transition SST model is adopted for all simulations which eventually increases the CPU time to about 22% whilst transition sensitive SST model formulation

is used to model the laminar separation bubble near the leading edge when boundary layer transits form laminar to turbulent state, because this LSB is a dominant phenomenon when characterizing pressure distribution, on-surface flow structure and wall shear stress over the wing and therefore the overall aerodynamic loads of the wing. However, even though SST $k-\omega$ is inefficient in correlating a good prediction of flow features at moderate Reynolds, it shows a comparative correlation with wind tunnel experiments at very high angles of attack.

The $\gamma-\tilde{Re}_{\theta,t}$ turbulence model still solves the transport equations for both k and ω quantities as $k-\omega$ SST does, which are otherwise identical with an exception for production, P_k and dissipation, D_k terms in kinetic energy (Eq.(1)) along with the blending function F_1 in specific dissipation rate (Eq.(2)) that controls the use of ω near the walls and ϵ far away. The production term, P_k is correlated with a turbulence intermittency, γ (Eq.(3)) bounded between values of 0 and 1, indicating physically the state of the flow locally by accounting for the percentage of time corresponding to the presence of turbulent fluctuations in the boundary layer. Where a value of 0 indicates that the flow is locally laminar hence close to the leading edge of the airfoil and when γ saturates to a value of 1 the flow is fully turbulent. Notice that freestream flow contains turbulent kinetic energy and specific dissipation rate, thus γ should have a value of 1 at inlet boundary condition and freestream so that it will be represented by the fully $k-\omega$ SST model. Regarding the dissipation term, Dk it is limited by a min max limiter (Eq.(4)) calibrated to ensure that its value does not drop below 10% of its fully turbulent value when $\gamma = 0$, because even when the boundary layer is laminar with no production of turbulent kinetic energy, if is there any turbulence the wall still dissipate it by damping these turbulent fluctuations of the flow. In other hand, numerical tweak is used to correct the blinding function, F_1 to prevent it to take a value of 0 in the laminar boundary layer near the wall where normally takes a value of 1 allowing the Transition SST model to take its $k-\omega$ form of $k-\omega$ SST turbulence formulation rather than $k-\epsilon$ which is ineffective in the near wall regions particularly when the values of y^+ are very small. Hence, the blending function is limited; to prevent it to switch accidentally to 0 in the laminar region; by a new term defined by an exponential decay of a Reynolds number like term (Eq.(5)) governed by a square-root of turbulent kinetic energy which is very small in the laminar portion of the boundary layer making this new term to tend to 1. In order to compute the values of γ in the flow field an additional standard transport equation for intermittency is solved (Eq.(6)). The production terms, P_γ is used to control the length of the transition region of the boundary layer by producing turbulent fluctuations and pushing γ to saturates at a value of 1 in the full turbulent region. This term takes the form of Eq.(7) characterized by two main terms F_{onset} and F_{length}, where the former is a switching function for the production of intermittency and the latter controls the rate of this production happens to be when Flength is large γ is produced quickly and saturates to 1 rapidly which shortens the length transition region. To assess the Fonset, the Transition SST model introduced another transported variable, $\tilde{Re}_{\theta,t}$ calculated everywhere in the computational domain (Eq.(8)). This variable connects the empirical correlations to the onset criterion of intermittency by calculating two local values $Re_{\theta,t}$ and $Re_{\theta,c}$ where transition occur and fluctuations begin to take place respectively. The source term, $P_{\theta,t}$ of Eq. (8) is included to force $\tilde{Re}_{\theta,t}$ to take its experimental value (proprietary of ANSYS-Fluent CFD code) specified at the inlet except near the wall where it is turned off allowing the freestream value of $\tilde{Re}_{\theta,t}$ to convect and diffuse toward the wall by introduction a blending function $F_{\theta,t}$ (Eq.(9)). Once $Re_{\theta,t}$ is computed F_{length} and F_{onset} are evaluated using algebraic relationships and when they are beyond certain threshold the source term, P_γ is switched on, hence production of intermittency γ will start for each cell ([21,22]).

$$\frac{\partial(\rho k)}{\partial t}+\nabla\bullet(\rho\mathbf{U}k)=\nabla\bullet\left[\left(\mu+\frac{\mu_t}{\sigma_k}\right)\nabla k\right] +P_k-D_k \tag{1}$$

$$\frac{\partial(\rho\omega)}{\partial t}+\nabla\bullet(\rho\mathbf{U}\omega)=\nabla\bullet\left[\left(\mu+\frac{\mu_t}{\sigma_k}\right)\nabla\omega\right]+\frac{\gamma}{\nu_t}P_k -\beta\rho\omega^2+2(1-F_1)\frac{\rho\sigma_{\omega_2}}{\omega}\nabla k:\nabla\omega \tag{2}$$

Where, $$\nabla k:\nabla\omega=\frac{\partial k}{\partial x_j}\frac{\partial\omega}{\partial x_j}$$

$$P_k\rightarrow P_k\,\gamma \qquad 0\leq\gamma\leq 1 \tag{3}$$

$$D_k\rightarrow D_k\,min\left[max\left(\gamma,\ 0.1\right),\ 1.0\right] \tag{4}$$

$$F_1,new=max\left(F_1,\ F_3\right) \tag{5}$$

$$\text{Where, } F_3 = e^{-(Re_y/120)^3} \quad \text{and} \quad Re_y = \frac{\rho y\sqrt{k}}{\mu}$$

$$\frac{\partial(\rho\gamma)}{\partial t} + \nabla\bullet(\rho\mathbf{U}\gamma) = \nabla\bullet\left[\left(\mu + \frac{\mu_t}{\sigma_\gamma}\right)\nabla\gamma\right] + P_\gamma - D_\gamma \tag{6}$$

$$P_{\gamma,1} = F_{length}\, C_{a1}\rho\, S\,(\gamma\, F_{onset})^{0.5}\,(1 - C_{e1}\gamma) \tag{7}$$

$$\frac{\partial\left(\rho\tilde{Re}_{\theta,t}\right)}{\partial t} + \nabla\bullet\left(\rho\mathbf{U}\tilde{Re}_{\theta,t}\right) = \nabla\bullet\left[\left(\mu + \frac{\mu_t}{\sigma_{\theta,t}}\right)\nabla\tilde{Re}_{\theta,t}\right] + P_{\theta,t} \tag{8}$$

$$P_{\theta,t} = 0.03\frac{\rho}{t}\left(Re_{\theta,t} - \tilde{Re}_{\theta,t}\right)(1 - F_{\theta,t}) \tag{9}$$

2.5 Boundary Conditions

In addition to the domain sensitivity analysis conducted to set right dimensions of upstream, downstream, top and bottom boundaries of the computational domain, an appropriate implementation of boundary conditions needs to be carefully considered. This is achieved by splitting the domain boundaries into three distinct regions, velocity inlet, pressure outlet downstream and symmetry side boundaries. A velocity inlet type was specified as Dirichlet boundary condition at inlet boundaries in such a way that freestream velocity is set to maintain a chord-based Reynolds number at 4.45×10^5. The used method for freestream turbulence is by setting values of turbulent kinetic energy and specific dissipation rate at the inlet boundary condition, unless otherwise stated, as $k = 2.53$ m^2.s^{-2}, $\omega = 151.55$ s^{-1} and an intermittency factor of 0.85 as dependence of flow features on γ values at the inlet was observed. These quantities are calculated based on empirical correlations related to SST $k-\omega$ turbulence model. The downstream domain boundary was prescribed as pressure-outlet boundary condition and set to a value of zero-gauge pressure as operating conditions of the working fluid are specified according to standard atmospheric pressure of 101.325 kPa and temperature of 288.15 K. In addition, an estimation of turbulent length scale of 10% the characteristic length is set at the pressure-outlet along with 5% backflow turbulence intensity. A stationary wall condition is adopted for both airfoil and rod surfaces with no-slip boundary condition, hence, no turbulence production from the wall itself to the freestream flow. The two side boundaries of the computational domain are assigned to symmetry boundary condition which enforces to null the normal component of all flow variables gradient by acting as zero shear slip wall. This condition seems to be satisfactory as the computational domain is large enough to maintain these far boundaries at constant static pressure (Fig.2).

2.6 Solver and Numerical Schemes

Ripley *et al.* [23] have shown that the laminar separation bubble does not involve any vortex shedding via their time-dependent numerical investigation of the laminar separated flow subjected to an adverse pressure gradient. As a motivation, three dimensional, incompressible, steady state, pressure based and segregated double precision numerical solver is adopted to conduct present simulations. All Steady RANS CFD runs were undertaken using the industry standard commercial CFD package known as $ANSYS^{©}$ - Fluent, Release 18.1. The code solves the Reynolds Averaged Navier Stokes equations in a finite volume environment with Message Passing Interface library parallelization. The Transition SST ($\gamma - \tilde{Re}_{\theta,t}$) four equations turbulence closure model is adopted to model the Reynolds stresses term. Pressure-Velocity field coupling is ensured using SIMPLE algorithm advantageous for problems requiring boundary layer high resolution. Spatial discretization of pressure term is treated by a standard interpolation scheme. Moreover, momentum diffusive terms, turbulent kinetic energy and specific dissipation rate equations are second-order central difference special discretization scheme and convection terms are treated using second-order upwind discretization scheme in space. Finally, the cell gradients of all variables are computed using weighted least square cell-based scheme. The initial flow field for all simulations is set according to predicted freestream inlet conditions. The different cases are computed for 50000 iterations where scaled residuals of all equations along with lift and drag coefficients of the wing are monitored to ensure adequate convergence. The overall computational time for every simulation to be converged was achieved in about 144 hours (wall clock) that led to reduction in the residuals of O(6).

3 Results and Discussions

Simulations of the flow around the wing at various angles of attack ranging between $[0^\circ - 24^\circ]$ for a chord-based Reynolds number of 4.45×10^5. are carried out for both baseline and controlled configurations in order to

Table 2 Lift coefficient from CFD simulations and wind tunnel experiments

	c_L **at** 10°	c_L **at** 12°	c_L **at** 14°
Present work	0.9035	1.0613	1.0876
CFD [24]	0.8752	0.9801	1.025
Error (%)	3.23	8.28	6.1
Exp.	0.898	1.021	0.962
Error (%)	0.61	4.0	13.05

understand how wing surface pressure are altered when a passive control method is introduced to enhance the overall wing aerodynamic performances at pre-stall and stall regimes.

3.1 Validation

For reason of results confidence, it is imperative to compare the obtained results from CFD simulations of the baseline wing with Wind Tunnel experiments to validate the numerical model adopted herein. Tests are carried out in an open jet closed circuit wind tunnel having circular test section of $600mm$ in diameter. The wing model is NACA 0012 airfoil based with $150mm$ chord length and $450mm$ span giving a maximum blockage ratio of 6.4%. The forces acting on the wing under the stream are measured by an aerodynamic balance composed of three parralel parts. The measurements range of each one is respectively $[-100N - +100N]$ for two of them and $[-50N - +50N]$ for the last one. A mechanism for angle of attack variation is also incorporated with the balance allowing α to bet set between $[-20^\circ - +40^\circ]$. The experiments for the baseline wing configuration used for CFD validation are obtained for a freestream velocity of 43.3 $\mathrm{m.s}^{-1}$, that corresponds to a Reynolds number based on the chord length of 4.45×10^5. The turbulence intensity for these flow conditions is 1%. Table 2 shows the error in the aerodynamic forces predicted by current numerical investigation when compared to CFD simulations of Huang *et al.* [24] and the wind tunnel results. It is noteworthy that deviations remain less than 8.28% in all instances except at 14° incidence where the wing stalls and making this region quite difficult to solve with turbulence modelling formulation of Navier-Stokes equations. Although simulations overpredict lift force coefficient the fact that the error is relatively consistent for each case, highlights that the overall trends shown by the numerical results are coherent with those occurring in the wind tunnel.

The distribution of the parietal dimensionless distance, y^+ on both wing surfaces and on the rod circumference have been computed. The average value is largely less than unity and is of the order of 10^{-1}. The maximum values are obtained at the leading edge separation point and are close to 0.7. Thus, resolution of the boundary layer of the flow near both bodies is performed accurately enough throughout the grid used to conduct the different CFD simulations. Hence, spacing of the first cell from the wall is validated for this numerical study.

3.2 Baseline Flow Analysis

Figure 3 shows the variation of the aerodynamic coefficients, c_L and c_D, at low Reynolds number and various angles of attack for the baseline NACA0012 wing simulations along with a schematic of the flow patterns observed for each representative state. It is noticed that, for incidence ranged between $[2^\circ - 13^\circ]$ a monotonous linear increase in the lift coefficient relatively growing in a constant rate up to a maximum value depicted at $\alpha = 13^\circ$. After reaching the peak, the value of c_L drops drastically at $\alpha = 14^\circ$ showing turbulent stalling phenomenon of the boundary layer taking place as clearly illustrated by the schematic of the streakline patterns on the wing surface. The flow separation is led to move upstream causing the wing to stall. Above incidence of $\alpha = 20^\circ$, the lift shows a tendency to be relatively constant. This is basically due to the main flow separation indicated by the presence of counter-rotating vortices on the suction side of the wing hence the post-stall is triggered. Regarding drag coefficient c_D, it remains almost unchanged for small angles of attack $[0^\circ - 6^\circ]$. Thereafter, it increases slightly in the meantime as the angle of attack is further changed possibly because of premature separation of the laminar boundary layer, followed by a significant rise for $\alpha = 14^\circ$ indicating presence of turbulent stall of the boundary layer. By further increasing the angle of attack, the drag coefficient continues growing till a maximum value is attained at incidence 24°.

The streamline close to the wing surface is presented in Fig.4. to make a comparison between various angles of attack and the presence of flow separation on the upper surface of the airfoil. It is believed that the nonlinearity in the lift curve slope is linked to presence of laminar boundary layer separation occurring at this low Reynolds number flow ($Re_c = 4.45 \times 10^5$). For an angle of attack between 0° to 8°, a separation bubble appears on the airfoil suction side that travels from the trailing edge to the leading edge as the incidence is increased, leading effectively to a change in location

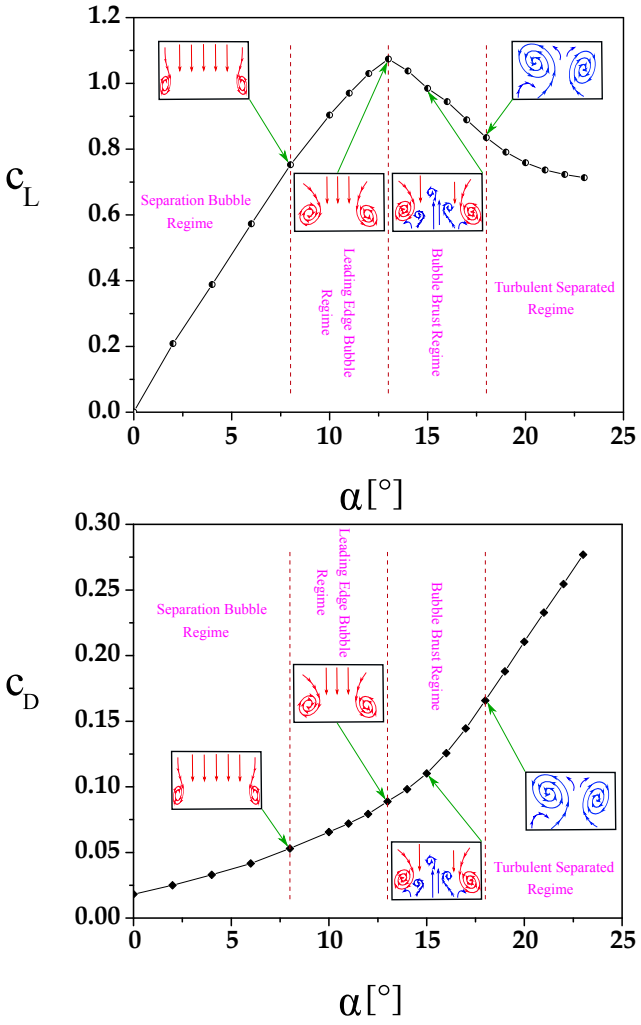

Fig. 3 CFD lift and drag coefficients for baseline case at varying AOAs.

of the transition line from laminar to turbulent states. For $\alpha > 8°$, two separate phenomena are observed consisting in presence of a conventional trailing edge separation bubble formed along with the first bubble near the leading edge as the angle of attack increases till the point of complete separation on the upper surface of the wing representing the stall phenomenon, at around an angle of attack of $[10° - 12°]$. These two phenomena can explain the change in lift curve slope observed in Fig.3.

3.3 Effect of Passive Control on LSB

Three-dimensional development of the LSB on the wing upper surface is inferred from average pressure distribution analysis on suction side presented in Fig.5. Showing mean pressure rapid increasing along the chordwise direction. It can be seen from colour contrasts of pressure distribution, existence of three distinguished regimes characterizing the zone of laminar separation bubble observed for low Reynolds number flow, namely, laminar, transient and turbulent flow regimes. These three regions are limited by the following three characteristic lines as shown in Fig.5: Laminar separation line; Transitional line and Reattachment line.

Effect of the passive control technique on development of the LSB is analysed and the most relevant results are presented in Fig.6. The figure depicts average pressure distribution contour on the upper surface of the wing at an incidence of $\alpha = 10°$. Comparing the two configurations side to side, baseline case and controlled case, it seems that the rod has significant influence on dimensions of the laminar separation bubble occurring on the suction side as a result of premature laminar boundary layer separation. Both regions, laminar and transitional, are influenced by presence of the rod wake. A significant reduction of approximately 50% in the laminar region is depicted by the three-dimensional average pressure distribution on the wing surface which yielding to a considerable enlargement of the transitional zone by approximately 30%. Thus, this vortex generator placed upstream the wing showed that LSB is extremely sensitive to the interaction between the rod wake and the airfoil leading to a bubble size reduction that is considered to be harmful for the wing overall aerodynamic performances. Therefore, a promising enhancement in aerodynamic characteristics will certainly contribute to improve efficiency of such wings operating at low Reynolds numbers.

3.4 Effect of Passive Control on Parietal Pressure Distribution

Figure 7 demonstrates both friction lines and average pressure distribution on the wing upper surface. When incidence is null ($\alpha = 0°$), friction lines on the wall surface are uniform and flows in the same direction as that of the main incoming flow, starting from the leading edge towards the trailing edge. As the angle of attack

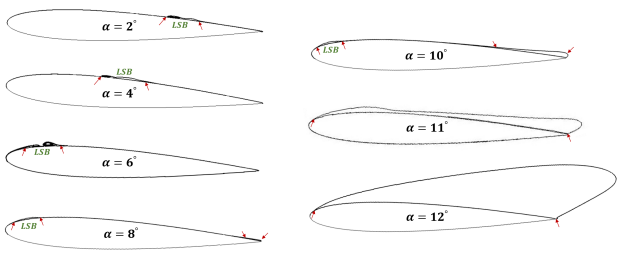

Fig. 4 Process of LSB migration at low Reynolds number of 4.45×10^5 for NACA0012 wing; arrows highlights the LSB location (flow moving left to right).

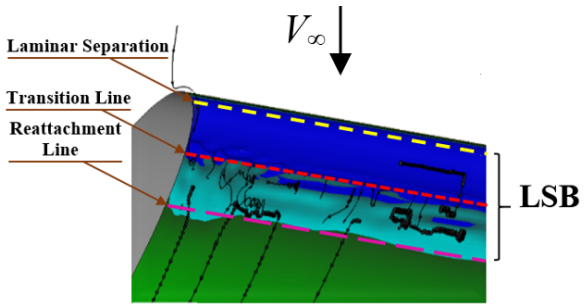

Fig. 5 LSB characterisation at flow conditions of $Re_c = 4.45 \times 10^5$ and $\alpha = 8°$ (flow moving top to bottom).

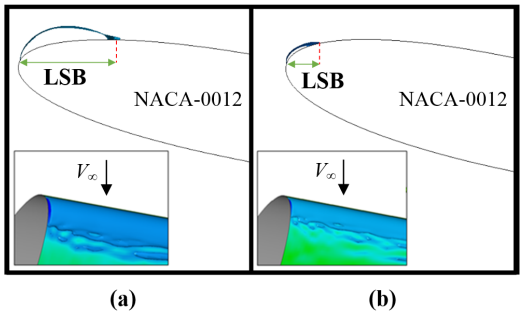

Fig. 6 Effect of microcylinder rod on LSB dimensions at $\alpha = 10°$; (a) baseline case; (b) controlled case (flow moving left to right).

is increased ($\alpha < 11°$), friction lines begin to loose their uniformity and smoothness behavior. An instability is triggered on both ends of the trailing edge, indicating presence of a partial separation of the boundary layer, developing progressively from the trailing edge towards the leading edge. Furthermore, the average pressure gradually increases in the chordwise direction starting from the leading edge. It begins with a zone of depression at the leading-edge level indicated by a uniform and homogeneous coloured zone and keeps growing to a high-pressure region at the trailing edge. For the baseline configuration at $\alpha = 11°$, the depression zone is narrow on both ends of the leading edge, because the instability generated between endplates and airfoil boundary layers mutually interact. This is much clearer through the friction lines distribution showing a pair of counter-rotating vortices swirling on the wing suction side. Consequently, partial turbulent stall of the main wing is triggered close to these regions. In case of controlled wing configuration, it shows, however, important changes noticeable on the mean pressure field as well as on the friction lines (Fig.7). Mainly, the depression region near the leading edge is getting uniformized in the spanwise direction starting from middle towards endplates. Another important outcome is revealed by new friction line patterns resulting from the control and consisting in the fact that the pair of vortices near endplates shrink in size making the incident flow more dominate on the wing surface. As a result, a reduction of about 56% on the overall drag force is reported for the controlled case. As the angle of attack is increased the instability amplifies more and more to form two large counter-rotating vortices covering a large part of the wing upper surface. A backflow is generated as a consequence of these two vortices. This reveals that energy of the incoming flow is more dominant than that of the backflow. As a result of this dominance the incident flow imposed its presence mainly in the midspan zone, hence, the boundary layer is not completely separated from the wing surface except in the region where the vortices are present. For $\alpha = 12°$, direction of friction lines on the midspan zone shows that the backflow becomes dominant and imposes its presence with respect to the incoming flow. The two counter-rotating vortices still exist, but larger in dimensions and intensities when compared to those observed for incidence $\alpha = 11°$. Therefore, secondary instabilities appear as a consequence of this interaction between the two flows of opposite sense and the significant energy of this backflow, Fig.8.In this case, the boundary layer is completely separated from the wall. This irregularity behind appearance of this instability disturbs the uniform distribution of the average pressure in both ends of the wing close to the leading edge. However, when flow control is applied, the average pressure distribution becomes uniform and homogeneous and the disturbed zones near the endplates vanish. In addition, this depression portion grows in size compared to previous angles. Moreover, presence of the rod has a significant impact on the flow developing on the wing suction side. From the Fig.8 it is easily noticeable that secondary instabilities reported before completely disappear and the incoming flow gained energy from the feeding vortex generator to become dominant over a large portion of the wing because it overpassed the early backflow seen without control. As a consequence, the tow counter-rotating vortices died out and straitened in size resulting a reduction in the drag force by 73% including the rod contribution. For incidence greater than 12°, the uniform distribution of the mean pressure over the entire upper surface is completely disturbed for the baseline configuration, Fig.9. Consequently, the flow within the boundary layer is completely unstable. The intensity of these instabilities increases with the angle of attack causing the so-called turbulent stall to launch. As α increases, these instabilities are intensified and the boundary layer separation is generalized to the entire

wing surface. For $\alpha = 13°$ the flow seems to behave in the same way as for 12° incidence without control. This is clearly shown by friction lines pattern, where the dominance of the backflow resulting from instabilities generated inside the boundary layer is well represented leading to secondary irregularities as a result of the interaction between the incident and back flows. In this case, the boundary layer is completely detached from the surface and this incident angle corresponds to the turbulent and massive stall angles of the flow. In the other hand, as the control technique is applied, the mean pressure distribution on the suction side of the wing exhibits a different behavior in comparison to the baseline case. As stated earlier, the mean pressure distribution is random due to partial separation of the boundary layer near endplates caused by the primary and secondary vortices that gain intensity to cover an important portion of the wing surface as illustrated in friction lines patterns showing dominance of the backflow over the incoming one. Thereby, presence of the vortex generator brought the depression zone near the leading edge from its randomness attitude to its uniform and homogenous shape similar to what was observed at lower angles of attack when control is absent. It is worthwhile noting from pressure contours that flow characteristics are delayed by 2° from the baseline configuration with flow control applied. In other words, the stall is postponed when the wing is operating in the rod wake. In fact, looking at the new pattern of friction lines after low control is set, what have been seen in average pressure distribution is emphasized throughout the assessment of the flow before and after the control. As a matter of fact, the wake produced by the rod evolves into shedded eddies interacting with the boundary layer developing on the wing upper surface in a way that they feed energy to the flow close to the wall from free-stream. Premature separated boundary layer is reinforced to overcome pressure gradients that is subjected to and stick again to the wall surface. Consequently, this phenomenon of energizing the upcoming flow is established by defeating the dominance of the backflow spotted in the baseline case, so that the flow recovered its chordwise direction mostly in the midspan portion of the wing. Although the pair of vortices remain near the endplates a part of consequence of three-dimensionalities attitude of the flow outcomes of interferences between the two boundary layers developing on either endplates and wing body, the secondary instabilities are completely vanished for the controlled case. To sum up this qualitative analysis that provides main differences on the flow structures before and after control, it is important to link these essential findings to their impact on aerodynamic loads specifically lift and drag forces. It is found that actual aerodynamic coefficients are highly sensitive to flow control in an extent of a lift enhancement of 17% to gather with a maximum drag reduction of 49% which is promising in a perspective of fineness improvement.

Figure 10 depicts mean surface pressure distribution on the suction side generated by the wing operating in the low Reynolds number condition and at 15° incidence angle. For the non-controlled case the surface pressures appear very instable, as expected, whilst at such high angle of attack a presence of an intense turbulent agitation of the flow within the boundary layer is naturally understandable as turbulent stall of the boundary layer has taken place. This is shown on the friction lines illustration (bottom right-hand column), which reveal in the low-pressure regions near endplates formation of a pair of counter rotating vortices due to circulation of flow from higher to lower pressure regions. Also, when looking at the evolution way of these lines going from the trailing edge towards the leading edge over the entire wing surface is an evidence on the backflow dominance over the incoming stream. Similarly, to what have been described in the previous angle of attack, the boundary layer is fully separated from the wing upper surface giving rise to a wing stalled state. In other hand, a micro rod is used for prospective wing performances enhancement. Some relevant findings are presented in the left-hand column of the Fig.10. The instabilities in the average pressure distribution seem to be damped down to an extent where uniformity and homogenous appearance is recovered close to the leading edge. An analogy of this pressure contour with the baseline case, turns up this flow pattern resulting from the control device is already seen at earlier angle of attack, 11°. This inferred that this passive control delays heavy stall by few degrees. There appear to be larger area of low pressure in the mid-span region of the wing as the main flow gain control over the backflow and sticks to the wing again through involvement of rod eddies that convey energy from free-stream to boundary layer. Whereas, close to the endplates, less suction is generated as the three-dimensional interfaces in the boundary layers of these two regions arise tiny secondary instabilities on both sides that block the flow from it. To complete what is said so far, friction lines on the upper surface of the wing at 15° incidence with flow control are also considered. It is found that the flow got back its streamwise direction in comparison to the baseline case. This is because the boundary layer is completely separated from the wall and reattach to the wing particularly in the mid-span region constraining the stream to flow downward to the trailing edge. Two thirds of the wing suction side are occupied by a

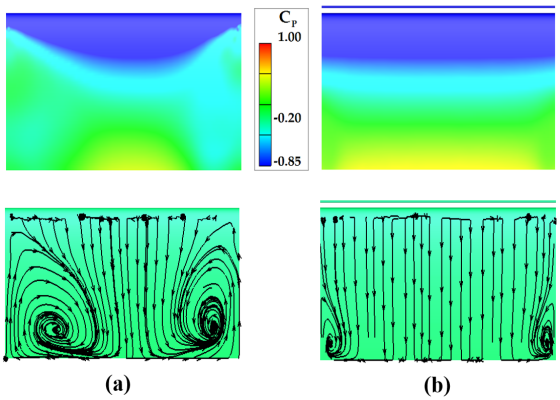

Fig. 7 Contours of pressure coefficient (upper column) and friction lines distribution (lower column) on wing suction side surface at flow conditions of $\alpha = 11°$ and $Re_c = 4.45 \times 10^5$; (a) baseline case; (b) controlled case (flow moving top to bottom).

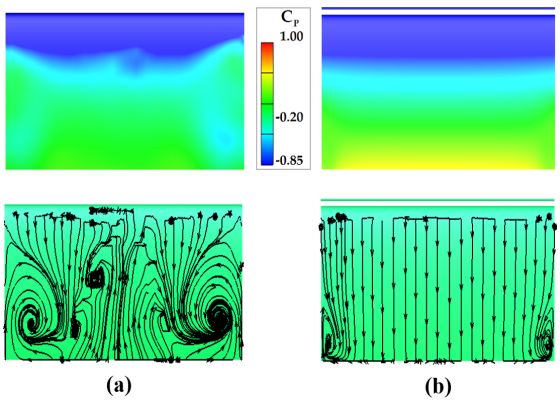

Fig. 8 Contours of pressure coefficient (upper column) and friction lines distribution (lower column) on wing suction side surface at flow conditions of $\alpha = 12°$ and $Re_c = 4.45 \times 10^5$; (a) baseline case; (b) controlled case (flow moving top to bottom).

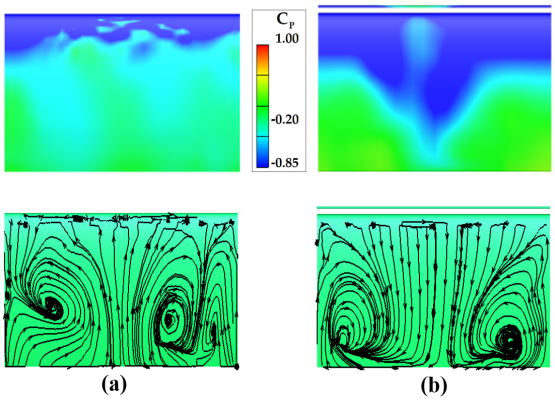

Fig. 9 Contours of pressure coefficient (upper column) and friction lines distribution (lower column) on wing suction side surface at flow conditions of $\alpha = 13°$ and $Re_c = 4.45 \times 10^5$; (a) baseline case; (b) controlled case (flow moving top to bottom).

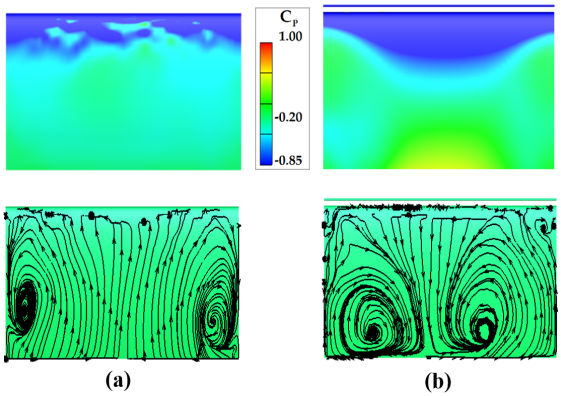

Fig. 10 Contours of pressure coefficient (upper column) and friction lines distribution (lower column) on wing suction side surface at flow conditions of $\alpha = 15°$ and $Re_c = 4.45 \times 10^5$; (a) baseline case; (b) controlled case (flow moving top to bottom).

pair of counter rotating vortices resulting from recirculation of the flow from high to low pressure. In addition of secondary instabilities close to the leading edge on both sides are generated the flow from the endplates interferes with the wing boundary layer, which yield it to partially stalled state. Finally, all these results conclusively show that passive control as uses here showed capability to delay full stall by 3°. Furthermore, an enhancement in aerodynamic loads is also ensured with control. 21% of drag reduction and 23% in lift growth are effectively obtained.

4 Conclusion

In this paper a passive flow control approach for a pre-stalled and post-stalled airfoil is numerically investigated. Flow response to placing a microcylindrical shaped rod near NACA-0012 wing-based profile at low chord-based Reynolds number of $Re_c = 4.45 \times 10^5$ is carefully examined. Particular focus is put on parietal pressure distribution on suction side surface along with flow field patterns with corresponding impart on the overall aerodynamic loads particularly high angles of attack ranging from 0° to 24°. The longitudinal gap between the wing and rod together with rod's diameter are key parameters carefully considered in this study. Detailed RANS CFD calculations are carried out for both controlled and baseline cases to show the influence of the joint device on the flow control effectiveness. Friction lines are further analyzed to give information on the flow field behavior on wall surface and correlative pressure distribution. The diameter of the

microcylindrical rod considered for this current study is $d/c = 0.013$, placed away from the wing leading edge at 3 times the diameter in the chordwise direction. For the baseline case, flow fields and average pressure coefficient distribution analysis made it possible to highlight the underlying physical phenomenology involved in laminar and turbulent boundary layer separation. It is shown that laminar boundary layer is particularly sensitive to pressure gradients induced by the wing at incidence. This caused premature separation of the flow followed by reattachment after transition to turbulent state accompanied by formation of the so-called laminar separation bubble (LSB). At the pre-stall flow condition ($\alpha < 13°$), the bubble forms near the trailing edge of the wing. As the incidence increases the LSB significantly decreases in length while migrating upstream to stabilize in the vicinity of the leading edge. This feature is encountered between $\alpha = 2°$ and $\alpha = 8°$. When the angle of attack is greater than 8°, the airfoil exhibits presence of a second conventional bubble near the trailing edge as well as the LSB near the leading edge. At $\alpha = 12°$ the laminar flow completely separates from the wing upper surface and forming a large recirculation zone; hence the wing is stalled. Any further increase in incidence results in the laminar separation bubble sudden burst leading to a heavy turbulent separation of the boundary layer subsequently to the important pressure gradient. Analysis of lift and drag forces with the LBS formed showed significant degradation in the overall aerodynamic loads pushing the wing to an abrupt stall. When the microcylindrical control device is introduced into the flow, a considerable influence on the behavior of the laminar separation bubble is induced. Presence of the rod revealed ability to partially eliminate the bubble by causing an early reattachment of the premature laminar separated boundary layer over a significant extent. The total length of the LSB is found to reduce by more than 75% and almost vanish for an incidence of 10°. Furthermore, the vortex like generator deeply impacts the flow structure especially at stall and post-stall conditions. At AOAs ranged between 10° to 15°, the control device acts similarly to a pumping system energizing the boundary layer on the airfoil counterbalancing the adverse pressure gradients. In fact, eddies generated in the cylinder wake interact with the boundary layer of the wing, ensuring convection of energy from freestream to near wall flow. The size of the downstream recirculation zone is significantly reduced for post-stall conditions. In other words, mean pressure contours and corresponding friction lines on the suction side are corroborating results for control effectiveness of the rod beyond stall conditions of the baseline wing. It was capable of maintaining attached flow for incidence of 15° till 33% of the whole wing upper surface close to the midspan region, while the backflow took advantage in non-controlled configuration, hence a complete separation from the leading edge was noticed. Finally, for pre-stall regime, the controlled flow doesn't provide significant improvement in either lift and drag, but does show effectiveness in reducing the length of the laminar separation bubble leading to further understanding of the intricate involved dynamics influencing the wing aerodynamic performances. Meanwhile, at post-stall regime presence of the rod close to the leading edge seems to effectively suppress or diminish and in most favorable case delay flow separation to higher angles of attack. This is advantageous to either lift enhancement or drag reduction, resulting respectively in a gain of 23% and a reduction of 73% as evaluated in this study.

References

1. Yang, Zhiyin and Voke, Peter R, Large-eddy simulation of boundary-layer separation and transition at a change of surface curvature. Journal of Fluid Mechanics 439: 305(2001).

2. Hain, R and others, Dynamics of laminar separation bubbles at low-Reynolds-number airfoils. Journal of Fluid Mechanics 630: 129(2009).

3. Zhang, Xuefeng and others, Hot-Film Measurements of Boundary Layer Transition, Separartion and Reattachment on a Low-Pressure Turbine Airfoil at Low Reynolds Numbers. 38th AIAA/ASME/SAE/ASEE Joint Propulsion Conference Exhibit: 3643(2002).

4. Tani, Itiro, Low-speed flows involving bubble separations. Progress in Aerospace Sciences 5: 70–103(1964).

5. Russell, John M, Length and bursting of separation bubbles: A physical interpretation of pressure distribution. Progress in Aerospace Sciences 5: (1979).

6. Hu, Hui and Yang, Zifeng, An experimental study of the laminar flow separation on a low-Reynolds-number airfoil. Journal of Fluids Engineering 130-5: (2008).

7. Gad-el-Hak, Mohamed, Flow control: passive, active, and reactive flow management. Cambridge university press: (2007).

8. Zhang, HJ and others, Aerodynamic Loading on a Cylinder behind an Airfoil. Experiments in fluids 38-5: 588–593(2005).

9. Zhou, CY and others, A Numerical Study of a Circular Cylinder in the Wake of an Airfoil. 15th Australasian Fluid Mechanics Conference, University of Sydney, Sydney, Australia: 13–17(2004).

10. Bajalan, S and others, Experimental Study of Frequency Behavior for a Circular Cylinder behind an Airfoil. World Academy of Science, Engineering and Technology,

International Journal of Mechanical, Aerospace, Industrial, Mechatronic and Manufacturing Engineering 5-11: 2356–2360(2011).

11. Shan, Hua and others, Numerical study of passive and active flow separation control over a NACA0012 airfoil. Computers & fluids 37-8: 975–992(2008).

12. Igarashi, Tamotsu, Enhancement of heat transfer and reduction of drag of a square prism in an air stream. International Heat Transfer Conference Digital Library: (1994).

13. Igarashi, Tamotsu,Drag reduction of a square prism by flow control using a small rod. Journal of Wind Engineering and Industrial Aerodynamics 69: 141–153(1997).

14. Igarashi, Tamotsu and Tsutsui, T, Enhancement of heat transfer and reduction of drag of a square prism arranged diamond-shape in an air stream. International Heat Transfer Conference Digital Library (1998).

15. Hafien, C and Bourehla, A and Bouzaien, M, Passive Separation Control on a Symmetric Airfoil via Elastic-Layer. Journal of Applied Fluid Mechanics 9-5: 2569–2580(2016).

16. Fan, TONG and Weiyang, QIAO and Weijie, CHEN and Cheng, Haoyi and Renke, WEI and Xunnian, WANG, Numerical analysis of broadband noise reduction with wavy leading edge. Chinese Journal of Aeronautics 31-7: 1489–1505(2018).

17. Supreeth, R and Arokkiaswamy, A and Anirudh, K and Pradyumna, RK and Pramod, PK and Sanarahamat, AK,Experimental and Numerical Investigation of the Influence of Leading Edge Tubercles on S823 Airfoil Behavior. Journal of Applied Fluid Mechanics 13-6: 1885–1899(2020).

18. Sefiddashti, Mehrdad Nafar and Nili-Ahmadabadi, Mahdi and Rizi, Behnam Saeedi, Experimental study of effects of circular-cross-section riblets on the aerodynamic performance of Risø airfoil at transient flow regime. Journal of Mechanical Science and Technology 32-2: 709–716(2018).

19. Durhasan, T., Passive Flow Control over an Airfoil by Control Rod at Low Reynolds Number. Journal of Applied Fluid Mechanics 13-6: 1819–1833(2020).

20. Norberg, C, LDV-measurements in the near wake of a circular cylinder. ASME Paper No. FEDSM98-521 41-5: (1998).

21. Langtry, Robin B and Menter, Florian R, Correlation-based transition modeling for unstructured parallelized computational fluid dynamics codes. AIAA journal 47-12: 2894–2906(2009).

22. Malan, P and Suluksna, K and Juntasaro, E, Calibrating the-re transition model for commercial cfd. AIAA Journal 1142: 53–57(2009).

23. Ripley, Matthew D and Pauley, Laura L., The unsteady structure of two-dimensional steady laminar separation. Physics of Fluids A: Fluid Dynamics 5-12: 3099–3106(1993).

24. Huang, L and others, Numerical study of blowing and suction control mechanism on NACA0012 airfoil. Journal of aircraft 41-5: 1005–1013(2004).